Measurements of Ocean Surface Backscattering Using an Airborne 94-GHz Cloud Radar—Implication for Calibration of Airborne and Spaceborne W-Band Radars

LIHUA LI

Goddard Earth Sciences and Technology Center, University of Maryland, Baltimore County, Baltimore, Maryland

GERALD M. HEYMSFIELD

NASA Goddard Space Flight Center, Greenbelt, Maryland

LIN TIAN

Goddard Earth Sciences and Technology Center, University of Maryland, Baltimore County, Baltimore, Maryland

PAUL E. RACETTE

NASA Goddard Space Flight Center, Greenbelt, Maryland

(Manuscript received 10 May 2004, in final form 8 October 2004)

ABSTRACT

Backscattering properties of the ocean surface have been widely used as a calibration reference for airborne and spaceborne microwave sensors. However, at millimeter-wave frequencies, the ocean surface backscattering mechanism is still not well understood, in part, due to the lack of experimental measurements. During the Cirrus Regional Study of Tropical Anvils and Cirrus Layers-Florida Area Cirrus Experiment (CRYSTAL-FACE), measurements of ocean surface backscattering were made using a 94-GHz (W band) cloud radar on board a NASA ER-2 high-altitude aircraft. This unprecedented dataset enhances our knowledge about the ocean surface scattering mechanism at 94 GHz. The measurement set includes the normalized ocean surface cross section over a range of the incidence angles under a variety of wind conditions. It was confirmed that even at 94 GHz, the normalized ocean surface radar cross section, σ_o, is insensitive to surface wind conditions near a 10° incidence angle, a finding similar to what has been found in the literature for lower frequencies. Analysis of the radar measurements also shows good agreement with a quasi-specular scattering model at low incidence angles. The results of this work support the proposition of using the ocean surface as a calibration reference for airborne millimeter-wave cloud radars and for the ongoing NASA CloudSat mission, which will use a 94-GHz spaceborne cloud radar for global cloud measurements.

1. Introduction

Clouds play a critical role in the earth's climate system. The vertical structure and spatial distributions of clouds are important in determining the earth's radiation budgets, which affect global circulations and ultimately climate. However, the lack of finescale cloud data is apparent in current climate model simulations (Houghton et al. 1995; Stephens et al. 1990). Millimeter-wave cloud radars have gained favor for measuring the spatial distribution of clouds because of their high scattering efficiency, low power consumption, and compact size. A number of airborne millimeter-wave cloud radars have been developed (Pazmany et al. 1994; Sadowy et al. 1997; Li et al. 2004). Meanwhile, a 94-GHz spaceborne cloud radar is in preparation for the National Aeronautics and Space Administration's

Corresponding author address: Lihua Li, NASA Goddard Space Flight Center, Code 912, Bldg. 33, Rm. C426, Greenbelt, MD 20771.
E-mail: lihua@agnes.gsfc.nasa.gov

(NASA) CloudSat program (Stephens et al. 2002). Another proposed spaceborne W-band cloud radar is the joint Japanese–European Earth Cloud, Aerosol and Radiation Explorer (EarthCARE) mission radar, as described by the European Space Agency (2001).

One challenge of using millimeter-wave radar for measuring clouds is achieving system calibration. The delicate nature of millimeter-wave components and the harsh environment in which they operate may cause undetected changes in the system response unless regular system calibration is performed. The calibration uncertainty specification of the CloudSat 94-GHz cloud radar is 2 dB (with a goal of 1.5 dB) (Stephens et al. 2002). Typically, a radar may utilize internal circuitry to monitor the variation of the power levels of the radio frequency (RF) transmitter and the drift of system gain, but characterization of the antenna, front-end waveguides, and the interfaces between these components, are not included with internal calibration. External calibrations using point targets, such as a trihedral corner reflector, have been performed for ground-based radars (Li et al. 2004; Sekelsky 2002). However, it is difficult to calibrate airborne or spaceborne radars using point targets due to the difficulty in separating the return of the calibration reference from background clutter.

The ocean surface has been widely used as a calibration target for airborne and spaceborne microwave radars and radiometers. Numerous studies of ocean surface backscattering have been performed at microwave frequencies (Jones et al. 1976; Plant 1977; Valenzuela 1978; Masuko et al. 1986). Based on experiences with operating millimeter-wave cloud radars on the ground and on airborne platforms, it will be essential to perform CloudSat radar calibration checks periodically once it is launched. The ocean surface could be a valuable calibration reference since there will be many measurement opportunities under clear-sky conditions. However, in part because of the lack of experimental measurements at millimeter-wave frequencies, the ocean surface backscattering mechanism is still not well understood. Meanwhile, attenuation caused by water vapor and oxygen absorption in the lower troposphere is significant at millimeter-wave frequencies. It is therefore necessary to correct this attenuation to reduce the uncertainty of the calibration. In addition to the radar calibration, the ocean surface return can also be used in estimating the path-integrated attenuation (PIA) along the radar beam. The PIA then is used as a constraint for retrieving radar attenuation, rain rate, or cloud particle microphysical properties (Meneghini et al. 1983; Iguchi and Meneghini 1994).

TABLE 1. CRS system specifications during CRYSTAL-FACE.

Frequency (GHz)	94.155
Peak power (kW)	1.7
PRF (kHz)	4/5 (dual PRF)
Pulse width (μs)	1.0
Transmit polarization	H
Receive polarization	V and H
Antenna beamwidth (°)	0.6 × 0.8
Antenna gain (dB)	46.4
Sensitivity (dBZ_e)*	−29 (from flight data)

* At 10-km range, 150-m range resolution, and 1-s averaging.

During July 2002, the Cloud Radar System (CRS), a 94-GHz (W band) pulsed-Doppler polarimetric radar developed by NASA Goddard Space Flight Center, was operated on a NASA ER-2 high-altitude (nominal 20 km) research aircraft in support of the NASA Cirrus Regional Study of Tropical Anvils and Cirrus Layers-Florida Area Cirrus Experiment (CRYSTAL-FACE) program (E. J. Jensen et al. 2003, unpublished manuscript). During the same experiment, the 9.6-GHz ER-2 Doppler Radar (EDOP; Heymsfield et al. 1996), dropsondes (Hock and Franklin 1999), as well as other remote sensors were also operated on the ER-2. Table 1 shows CRS system parameters during CRYSTAL-FACE. The radar calibration was performed using a trihedral corner reflector after CRYSTAL-FACE. The calibration result was verified by side-by-side intercomparison with the University of Massachusetts (UMass) ground-based Cloud Profiling Radar System (CPRS) 95-GHz cloud radar (Sekelsky and McIntosh 1996), which has been well maintained and calibrated over the past decade. Intercomparison measurements between the CRS and CPRS for similar cloud volumes were conducted during autumn 2002. Figure 1 shows a comparison of CRS and CPRS W-band radar reflectivity profiles. The mean difference of the profiles computed over the range gates within clouds is within 1 dB. The details of the CRS hardware, installation on ER-2, system calibration, and preliminary cloud measurements from CRYSTAL-FACE are described by Li et al. (2004) and McGill et al. (2004).

During CRYSTAL-FACE, the ocean surface backscattering was measured by CRS over the southern Florida offshore region. The radar measurements are used to investigate the efficacy of using ocean surface returns as references for calibrating airborne and spaceborne W-band radars. This paper describes the CRS measurement concept on ER-2 and presents CRS ocean surface backscattering measurements obtained from CRYSTAL-FACE. Section 2 starts with the radar

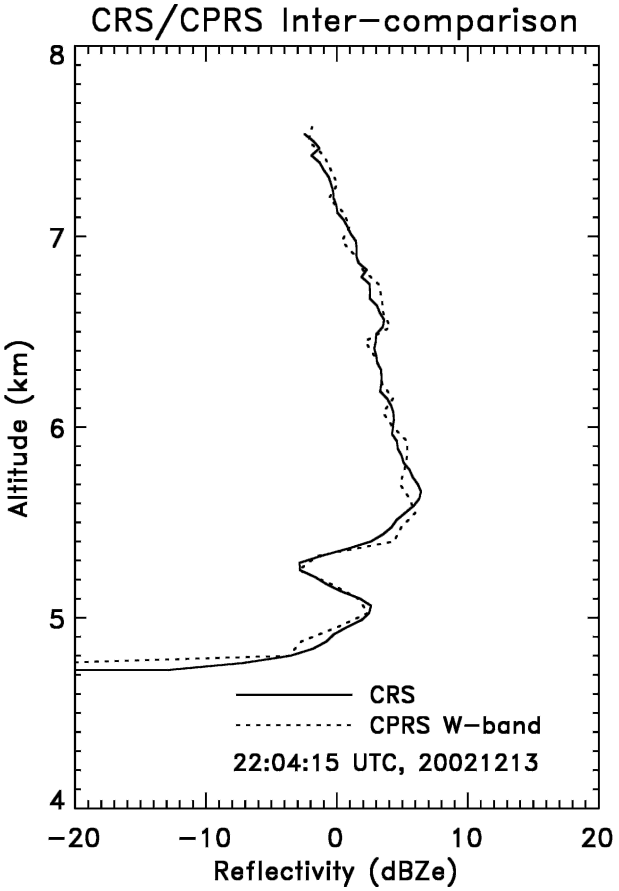

FIG. 1. CRS intercomparison with CPRS W-band radar at UMass, 13 Dec 2004. The mean difference between the two profiles is within 1 dB.

range equation of ocean surface scattering, discusses the need to correct for atmospheric attenuation at 94 GHz, and introduces the ocean surface backscatter model using three parameterizations of the mean surface slope. Section 3 explains the configuration of the instrumentation during CRYSTAL-FACE and describes the dataset used in this study. Section 4 presents CRS measurements and compares these measurements with EDOP data and model predictions.

2. Background

a. Radar equation of ocean surface scattering

The basic form of a radar equation for surface scatter is given by (Kozu 1995)

$$P_r = \frac{10^6 P_t G_a^2 \lambda^2 \sigma_o \beta\varphi \cos(\theta)}{512 \ln 2 \pi^2 l_r l_{\text{tx}} l_{\text{atm}}{}^2 h^2}, \quad (1)$$

where

P_r = power at the receiver (mW),
P_t = peak transmit power (kW),
G_a = antenna gain,
λ = radar signal wavelength (m),
β, φ = antenna 3-dB beamwidth in the horizontal and vertical (radians),
l_r = loss between the antenna and receiver port,
l_{tx} = loss between the transmitter and the antenna port,
l_{atm} = one-way path-integrated atmospheric attenuation
θ = radar beam incidence angle (radians),
σ_o = normalized ocean surface radar cross section, and
h = altitude of the aircraft (m).

The product of $P_t\ G_a\ \lambda^2\ \beta\ \varphi/l_r\ l_{\text{tx}}$ only depends on the radar system parameters. This product is related to the radar constant such as that used by Sekelsky (2002):

$$R_c = \frac{1024 \ln 2 \lambda^2 l_{\text{tx}} l_r 10^{21}}{P_t G_a^2 c \pi^3 \tau \beta \varphi}, \quad (2)$$

where c is the speed of light (3×10^8 m s^{-1}) and τ is the RF pulse width (s.)

The value of R_c can be evaluated from 1) measurements of individual parameters in (2); 2) an external calibration using a target with known radar cross section, such as a trihedral corner reflector (Sekelsky 2002); and 3) the ocean surface. For our case, R_c for the CRS was obtained from a series of external calibrations using a trihedral corner reflector (Li et al. 2004) as mentioned earlier. Assuming that a beam-filled condition is satisfied, σ_o can be calculated as

$$\sigma_{\text{o}} = \frac{P_r c \pi^5 l_{\text{atm}}^2 \tau R_c h^2}{2\lambda^4 10^{21} \cos(\theta)}. \quad (3)$$

On the other hand, if the ocean surface conditions and σ_o are known, the radar constant can be derived from (3) so that radar calibration is achieved. In section 4, observational estimates of σ_o and their dependence on the radar beam incidence angle and surface wind conditions are examined.

b. Attenuation due to atmospheric absorption

Water vapor and oxygen absorption at millimeter-wave frequencies is much stronger than at microwave

frequencies (Lhermitte 1988; Clothiaux et al. 1995; Li et al. 2001). Because water vapor and oxygen are highly concentrated in the lower troposphere, ocean surface measurements made from an airborne or spaceborne radar are attenuated by their presence. For tropical and midlatitude regions the attenuation can be significant. In subtropical ocean areas such as Florida, the two-way path-integrated attenuation from water vapor and oxygen absorption can be as high as 7.5 dB as a result of the high humidity and high temperature. A practical atmospheric millimeter-wave propagation model developed by Liebe (1985) predicts attenuation and path delay of moist air for frequencies up to 1000 GHz. The input variables of this model are height distributions (0–30 km) of pressure, temperature, and humidity along the propagation path. Using profiles of relative humidity, temperature, and pressure measured by the ER-2 dropsondes and radiosondes launched from the surface, the attenuation has been estimated and corrected using Liebe's (1985) millimeter-wave propagation model.

c. Ocean surface backscatter model

In general, σ_o is a function of radar wavelength, radar beam incidence angle, polarization, ocean surface wind speed, and wind direction. For incidence angle θ smaller than 15°, σ_o is dominated by large-scale surface waves, and at microwave frequencies the quasi-specular scattering theory has been shown to work well in this region (Valenzuela 1978; Barrick 1974; Brown 1990). When θ is larger than 15°, Bragg scattering produced by small-scale waves becomes more significant, and therefore, two-scale or multiscale models have been used since they take into account both quasi-specular scattering and Bragg scattering (Brown 1978; Chan and Fung 1977; Plant 2002). For the CRS operating on the NASA ER-2 and for the CloudSat radar, the primary measurement objective is to obtain vertical profiles of cloud and precipitation layers. Therefore, these radars are designed to operate at low incidence angles and the quasi-specular scattering theory is considered valid. Under this theory, the ocean surface is assumed isotropic and the surface wave distribution probability density is only a function of the surface mean-square slope, $s(\upsilon)$; σ_o is then approximately given as (Valenzuela 1978; Brown 1990)

$$\sigma_o(\theta, \upsilon, \lambda) = \frac{|\Gamma_e(0, \lambda)|^2}{s(\upsilon)^2 \cos^4(\theta)} \exp\left[- \frac{\tan^2(\theta)}{s(\upsilon)^2} \right], \quad (4)$$

where λ is the radar wavelength, υ is surface wind speed in meters per second, and $s(\upsilon)^2$ is the effective mean-square surface slope. The ocean surface effective Fresnel reflection coefficient at normal incidence is $\Gamma_e(0, \lambda) = C_e[n(\lambda)-1.0]/[n(\lambda) + 1.0]$ and $n(\lambda)$ is the complex refractive index for seawater. For the CRS operating frequency, n ($\lambda = 3$ mm) $= 3.36-j1.93$, where j is the imaginery part of a complex number, at 20°C (Meneghini and Kozu 1990). The Fresnel reflection coefficient correction factor, $C_e = 0.88$, is discussed in the appendix. It is worth noting that this quasi-specular theory cannot resolve the dependency of σ_o on wind direction.

The effective mean-square surface slope, $s(\upsilon)^2$, is given by different empirical relationships. Cox and Munk (1954) developed a linear relationship based on classical optical scattering data. They showed that $s(\upsilon)^2 = 0.003 + 5.08 \times 10^{-3}\upsilon$, varied linearly with wind speed for both a low-pass filtered surface where only gravity waves are present, and a "clean" surface, which includes capillary wave scale roughness. Wu (1972, 1990) reanalyzed the data obtained by Cox and Munk (1954) and showed that the mean-square slope varies approximately with the logarithm of wind speed. Therefore, $s(\upsilon)^2$ is expressed as $s(\upsilon)^2 = w_0 + w_1 \log_{10}(\upsilon)$, where w_0 and w_1 are empirically determined constants, but different in two wind speed regimes: for $\upsilon < 7.0$ m s^{-1}, $w_0 = 0.009$ and $w_1 = 0.0276$; for $7.0 < \upsilon < 20.0$ m s^{-1}, $w_0 = -0.084$ and $w_1 = 0.138$. Based on the statistical analysis of the σ_o measurements obtained by the Tropical Rainfall Measuring Mission (TRMM) K_u-band (13.8 GHz) precipitation radar and surface wind measurements obtained by the passive TRMM Microwave Imager, Freilich and Vanhoff (2003) derived $w_0 = 0.0036$ and $w_1 = 0.028$ for $1.0 < \upsilon < 10.0$ m s^{-1}, and $w_0 = -0.0184$ and $w_1 = 0.05$ for $10.0 < \upsilon < 20.0$ m s^{-1}. In the following, these three surface slope relationships are discussed and compared with radar measurements from CRYSTAL-FACE.

3. Data description and processing

a. Radar configuration during CRYSTAL-FACE

During CRYSTAL-FACE, the CRS was installed in the tail cone of the ER-2 right wing superpod, while EDOP was operated from the nose of the ER-2. Figure 2 illustrates CRS measurement geometry during CRYSTAL-FACE. The CRS was configured in a fixed nadir-pointing mode and its incidence angle changed when the ER-2 made turns. The incidence angle of the

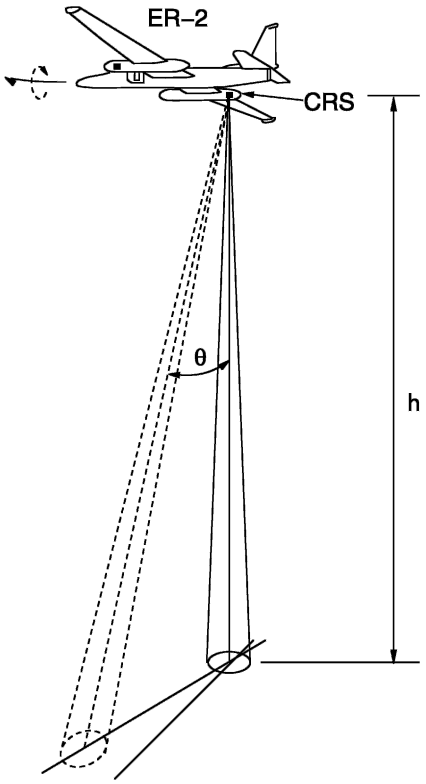

FIG. 2. Geometry of the CRS measurements from NASA ER-2 during CRYSTAL-FACE. The CRS was installed in a nadir-looking mode. The radar beam was scanned in a cross-track direction when ER-2 rolled its body to one side during turns.

radar beam, θ, is derived using aircraft pitch-and-roll angles, which are provided by the aircraft navigation system at an 8-Hz rate and simultaneously recorded along with the 2-Hz radar data. The accuracy of the aircraft pitch and roll is 0.05°. Ideally, the radar beam should be pointed along nadir. However, during installation, alignment errors result in offsets of the radar beam from nadir in both pitch and roll. These offsets are estimated and corrected using σ_o and Doppler velocity measurements of the ocean surface. The offset in pitch (along track) was obtained using the Doppler velocity of the ocean surface, which should be 0 m s^{-1} on average. Using this method, the CRS antenna-pointing uncertainty was determined to be about 0.2° in pitch. The offset in roll (cross track) was estimated by comparing σ_o measurements from right and left turns. At low incidence angles, σ_o versus θ curves measured from right and left turns should agree with each other since σ_o is not sensitive to wind direction at low incidence angles (Jones et al. 1976). The CRS beam offset in roll was determined to be less than 0.4° (see section 4a and Fig. 8).

The CRS antenna has an elliptical beam with a beamwidth of 0.6° cross track and 0.8° along track. The ER-2 flew at a nominal 20-km altitude; therefore, the CRS footprint size on the surface was 210 m cross track and 280 m along track. The RF pulse width of the CRS was 1.0 μs (150 m in range), and data were averaged for 0.5 s before being stored onto a solid-state recorder. With the 1.0-μs pulse width, the surface footprint is beam filled up to a 32° incidence angle. During the CRYSTAL-FACE flights, the maximum radar beam incidence angle was less than 30° when the aircraft made turns. Therefore, all CRS measurements from this experiment were valid for the beam-filled condition. Meanwhile, the CRS data were sampled at a 0.25-μs time interval (37.5-m range spacing), and the ocean surface return was oversampled by a factor of 4. Oversampling significantly reduces the error of the surface return power (Kozu et al. 2000; Caylor et al. 1997).

In this study, measurements of σ_o made by CRS are compared to the measurements made by the 9.6-GHz EDOP, which has two beams: one pointing to nadir and the other pointing to 33° forward from nadir. Here the EDOP is used as an independent source to verify CRS ground surface calibration results since the EDOP has been well calibrated using the TRMM precipitation radar and ocean surface return (Heymsfield et al. 1996, 2000). The beamwidth of the EDOP nadir beam antenna is 2.9°, about 4 times that of the CRS beamwidth. The RF pulse width and sampled gate spacing of EDOP are 0.5 μs (75 m in range) and 37.5 m, respectively. For this operating mode, the beam-filled approximation is only valid for incidence angles smaller than 5°. Therefore, σ_o measured by the EDOP nadir beam is calculated using the "partially beam-filled" equation [Eq. (16) in Kozu (1995)] so that it is comparable to the CRS data. The measurement of σ_o from EDOP was oversampled by a factor of 2.

b. *Atmospheric attenuation estimation and surface wind speed*

Sounding data profiles, used to estimate atmospheric attenuation, were obtained by the ER-2 GPS dropsondes (RD-93 model) developed by the National Center for Atmospheric Research (NCAR; Hock and Franklin 1999). They provided pressure, temperature, humidity, and surface horizontal wind, etc. The measurement accuracies of these dropsondes are pressure, ±1.0 hPa; temperature ±0.2°C; humidity, ±7%; and horizontal wind, ±0.1 m s^{-1}. During CRYSTAL-FACE, between four and eight

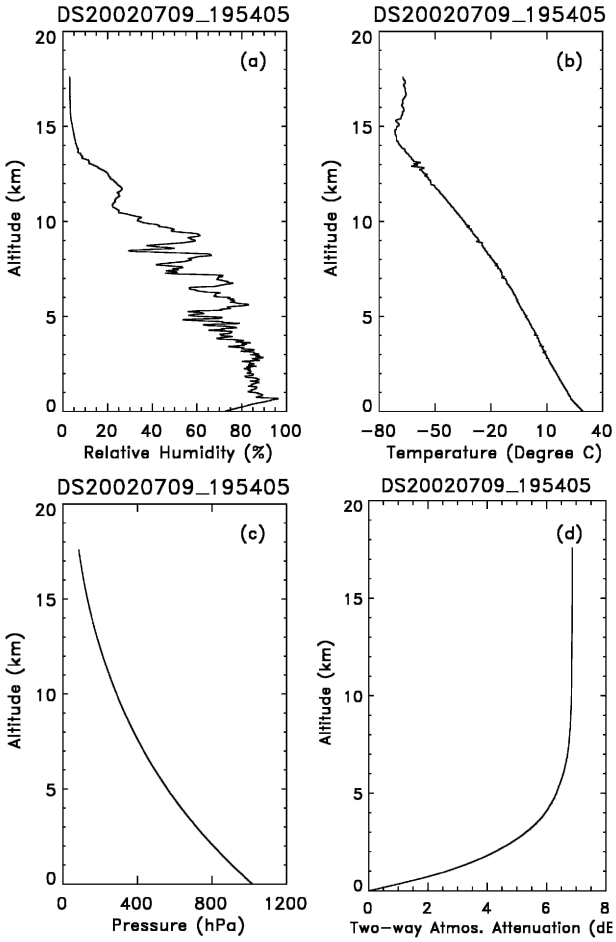

FIG. 3. Dropsonde measurements at 1954 UTC 9 Jul 2002: (a) relative humidity, (b) temperature, and (c) pressure. (d) The two-way cumulative path attenuation due to water vapor and oxygen absorption at 94 GHz.

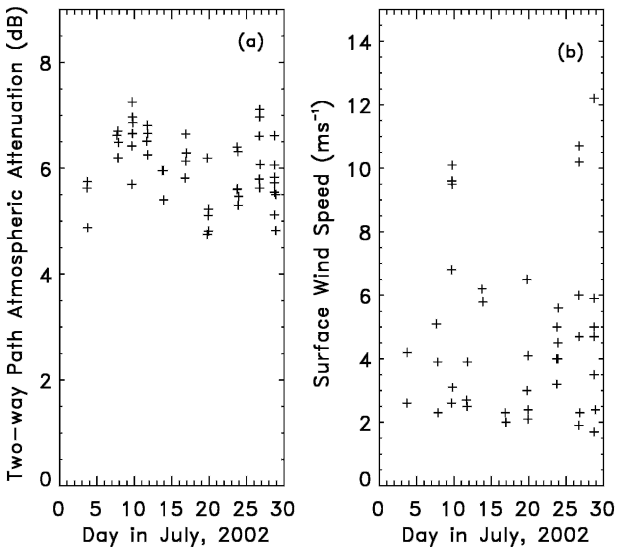

FIG. 4. (a) Two-way PIA due to water vapor and oxygen absorption at 94 GHz derived from dropsonde data collected from CRYSTAL-FACE. It shows the PIAs with a mean of 5.8 dB and a standard deviation of 0.65 dB. (b) Ocean surface wind speed measured by dropsondes during CRYSTAL-FACE.

dropsondes were typically launched during each 5-h flight. Figure 3 shows temperature, relative humidity, and pressure profiles measured by a dropsonde from clear-sky conditions at 1954 UTC 9 July 2002. The latitude and longitude of the dropsonde launch point were 23.83°N and 86.15°W, respectively. The estimated two-way PIA due to water vapor and oxygen absorption is shown in Fig. 3d. For this case, the maximum two-way PIA is 6.7 dB.

The ER-2 flew 11 science missions during the experiment in which about 50 dropsondes were launched. Figure 4a shows the two-way PIA due to water vapor and oxygen absorption under clear weather condition. The results show that the averaged two-way-integrated water vapor and oxygen attenuation is approximately 5.8 dB with a standard deviation of 0.55 dB. The high attenuation and large standard deviation reveal the importance of the correction of ocean surface measurements for atmospheric attenuation. In addition to the near-surface measurements made by the dropsondes, ocean surface wind measurements were obtained from nearby surface buoys as well. Figure 4b shows the surface wind speed measured by ER-2 dropsondes during CRYSTAL-FACE. The measurements indicate that the ocean surface wind speed was between 1 and 7 m s^{-1} for most ER-2 flights.

4. σ_o observed by the CRS

a. σ_o versus incidence angle

On 9 July 2002, the ER-2 flew a tropical cirrus mission from its base at Key West, Florida, through the Yucatan Channel, then south-southeast into the Caribbean Sea (Fig. 5). On the return trip, the ER-2 made a turn through point B (1935 UTC, 21.72°N, W86.11°W) under clear weather. During the turn, the CRS radar beam scanned along the cross-track direction away from and back to nadir. Figure 6 shows σ_o measured by CRS versus the incidence angle compared with theoretical curves. The σ_o measured by EDOP is also shown in Fig. 6 as diamonds. Figure 6 shows a larger variation in EDOP measurements, which were oversampled by a factor of 2 than the CRS measurements, which was oversampled by a factor of 4. This observation is con-

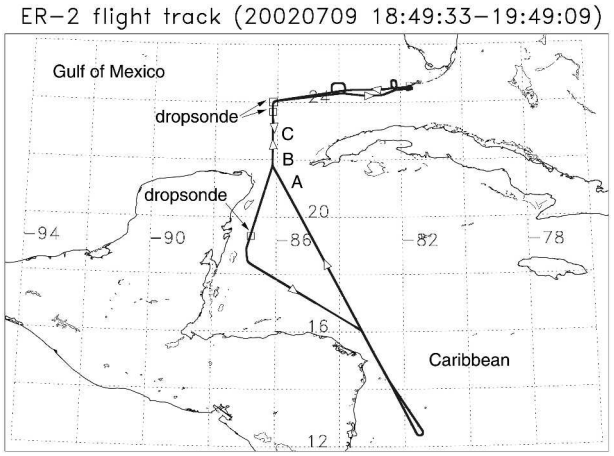

FIG. 5. ER-2 flight track on 9 Jul 2002. It shows three dropsonde launching positions near the ER-2 turning point B.

sistent with the results reported by Caylor et al. (1997) and Kozu (1995), and indicates that the errors in σ_o estimates can be reduced by oversampling along the radar range.

It is difficult to obtain the exact surface wind conditions at turn point B, but measurements were made by dropsondes launched at 1601 UTC (23.75°N, 86.16°W), and at 1644 UTC (19.01°N, 86.91°W) on the outbound trip, and at 1954 UTC (23.83°N, 86.16°W) on the return trip (see locations in Fig. 5). The near-surface wind speeds measured by these dropsondes were 2.6, 3.1, and 6.8 m s^{-1}, respectively. Results using the models described in section 2 with wind speeds of 2.5, 3.0, and 6.5 m s^{-1} are plotted for comparison in Fig. 6. In Fig. 6a, the CRS measurements fall between the 2.5 and 6.5 m s^{-1} Cox and Munk model predictions, and they are closest to the 3.0 m s^{-1} curve for $\theta < 15°$. However, near a 10° incidence angle, the CRS measurements (~6 dB) agree well with the model results for the three wind speeds. For EDOP, only the 3.0 m s^{-1} Cox and Munk model result is plotted. Figure 6b shows that both the CRS and EDOP measurements match well with Wu's (1990) surface slope relationship for 3.0 m s^{-1} wind speed up to 12° incidence angle. For incidence angles larger than 12°, Bragg scattering produced by small-scale waves becomes more significant, and thus, two-scale or multiscale models have to be used (Barrick 1974; Brown 1978; Plant 2002). Similarly, Fig. 6c shows radar measurements and model results using the surface slope relationship from TRMM data. For the same surface wind speed, TRMM's surface slope relationship predicts higher σ_o for low incidence angle (<10°), and more rapid decrease of σ_o along with an increase of the incidence angle. For this case, radar measurements are closest to the 6.5 m s^{-1} curve. It is worth noting that near a 10° incidence angle, all three surface slope relationships predict pretty much the same σ_o values for different wind conditions and the model results agree with the CRS measurements (~6 dB) well at this incidence angle.

On 26 July 2002, the ER-2 flew a pattern to the Caribbean Sea similar to that on 9 July. Figure 7 shows a portion of the flight track near two directional turns, with an insert of the full flight pattern. The aircraft flew almost identical tracks on the outbound and return trips. Similar to Fig. 6, Fig. 8 shows σ_o versus incidence angle during the turns close to way point F. For the outbound trip, the ER-2 flew through E, F, and G at 1721 UTC, and σ_o is shown in Fig. 8 as a plus sign (+). During the return trip, the ER-2 flew through G, F, and E at 1956 UTC, and the corresponding curve is presented by an open diamond (◊) in Fig. 8. Surface wind speed measured by dropsonde was 2.5 m s^{-1} at 1753 UTC (18.51°N, 84.48°W), and 2.3 m s^{-1} at 2017 UTC

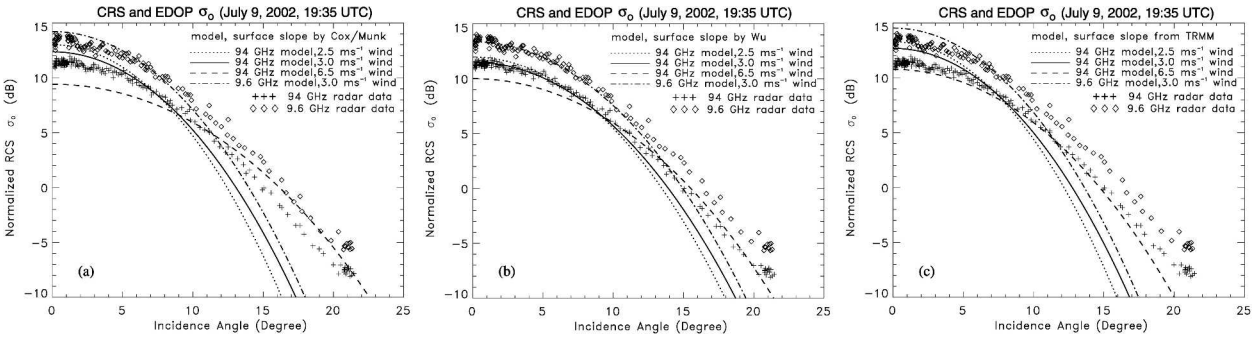

FIG. 6. The σ_o measured by the CRS vs incidence angle during the turn shown in Fig. 5, and compared to the quasi-specular model with 2.5, 3.0, and 6.0 m s^{-1} wind speeds as well as using (a) Cox and Munk's (1954), (b) Wu's (1972, 1990), and (c) TRMM's surface slope relationships. For comparison, EDOP data and model predictions at 9.6 GHz and 3.0 m s^{-1} wind are also shown in each figure.

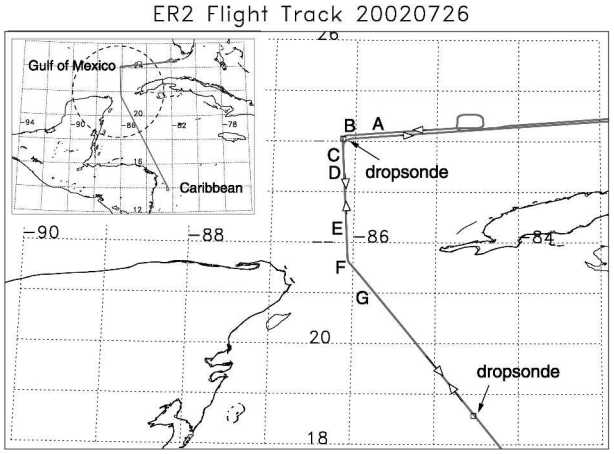

FIG. 7. ER-2 flight track on 26 Jul 2002. A larger-scope plot is shown at the upper left-hand corner. ER-2 flew the track on its outbound trip and on its return trip. It made turns at way points B and F.

(24.0°N, 86.15°W). The quasi-specular models using different surface slope relationships with 2.5 m s^{-1} surface wind speed are shown by the curves in Fig. 8. It is evident that radar measurements from the outbound turn and return-trip turn agree very well even though they were 2.5 h apart in time. At a low incidence angle, radar measurements match well with model results and are in closer agreement with Wu's (1972, 1990) relationship than the other two. It is worth noting that although the models are "tuned" using C_e, which is estimated from CRS measurements, the shape of σ_o versus θ curve will not be affected by possible errors in C_e since these errors only result in offsets in the σ_o.

Other turn events from different days of the experiment were also used to calculate σ_o as a function of incidence angle. Figure 9 shows σ_o versus incidence angle from 12 clear weather cases. Each case is indicated by a different letter. The different dependencies of σ_o with incidence angle are due to differences in ocean surface structure attributed to different surface winds. Results from the quasi-specular model with three different surface slope relationships and with 1.25 and 8.0 m s^{-1} wind speeds, are plotted for comparison. It is noteworthy that near the 10° incidence angle, σ_o measurements are less sensitive to wind speed, which also agrees with the quasi-specular model and measurements obtained at lower microwave frequencies (Jones et al. 1976; Plant 1977; Masuko et al. 1986). At 10° incidence angle, the mean value of the measured σ_o is 5.85 dB with a standard deviation of 0.6 dB.

b. Effects of wind speed and direction on σ_o

Figure 10 presents measured σ_o at 3°, 10°, and 15° incidence angles versus ocean surface wind speed. Results using the quasi-specular model and three different surface slope relationships are also shown for comparison. The discrepancy between the radar measurements and model results is likely due to (a) the uncertainty

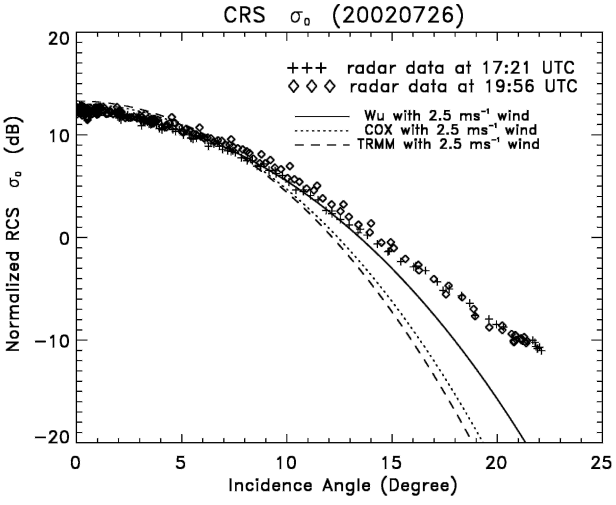

FIG. 8. The σ_o measured by the CRS vs incidence angle from the turns near way point F shown in Fig. 7. Crosses represent measurements from the outbound turn through E, F, and G consequentially. Diamonds represent measurements from the turn through G, F, and E on the return trip consequentially.

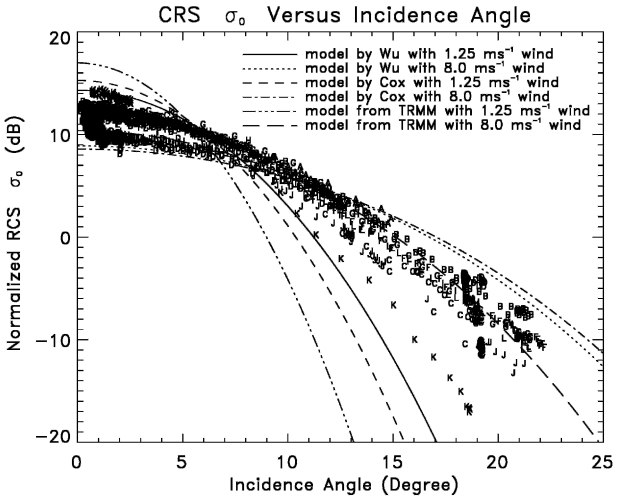

FIG. 9. The σ_o measured by the CRS vs incidence angle from different turns made in different days. A total of 12 turns from clear weather is shown.

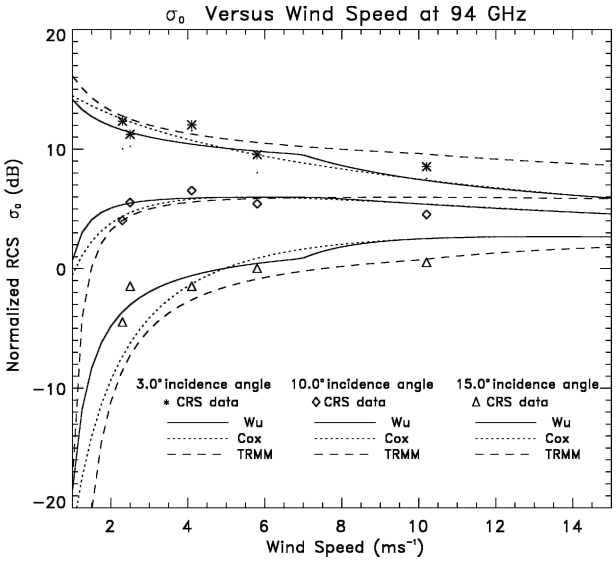

FIG. 10. The σ_o vs ocean surface wind speed at different incidence angles. Results from the quasi-specular scattering model are shown as the solid, dotted, and dashed lines.

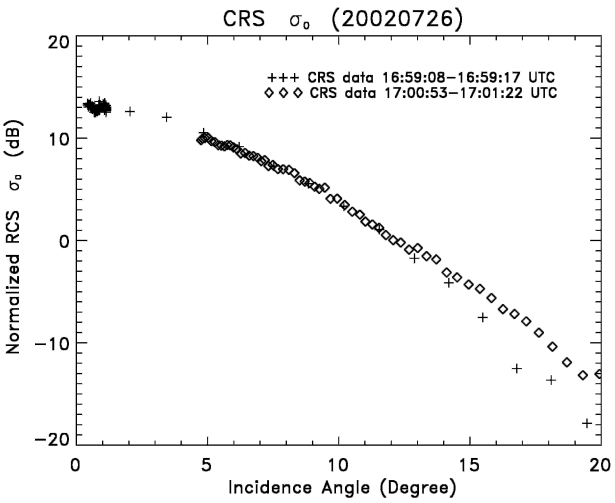

FIG. 11. The σ_o from a turn with a 100° heading change, which indicates that σ_o varies relative to wind direction for an incidence angle larger than 12°.

of the wind speed estimate caused by a collocation error between the radar beam footprint on the ocean surface and the dropsonde fall position at the surface, (b) an error in the estimates of the water vapor and oxygen attenuation, and (c) possible errors in the model.

Measurements at microwave frequencies have shown that not only the wind speed, but also the wind direction and polarization of the radar beam affect scattering from the ocean surface. Jones et al. (1976) showed that σ_o were slightly different for upwind, downwind, and crosswind conditions at a low incidence angle. However, this difference becomes more significant when incidence angles are larger than 15°. During CRYSTAL-FACE, the CRS transmit polarization was such that the *E*-field was perpendicular to the direction of flight, therefore the radar signal was vertically polarized (V plane) relative to the ocean surface during the turns.

For the 26 July case shown above, the ER-2 made nearly a right angle turn at 1700 UTC during the outbound flight (through A, B, C, and D in Fig. 7). A dropsonde, launched at 2117 UTC on the return trip, measured a surface wind speed of 2.3 m s^{-1} from 211°. Figure 11 presents σ_o versus incidence angle during the turn. The radar beam was oriented upward and slightly to the right of the wind in the first half turn [shown by a plus sign (+) in Fig. 11] and then changed over to the left of the wind in the second half of the turn [shown by an open diamond (◊) in Fig. 11]. For an incidence angle larger than 12°, the discrepancy of σ_o between the first half and second half of the turn is evident.

From 1731:38 to 1734:29 UTC on 29 July 2002, the ER-2 performed a 250° clockwise turn in azimuth while maintaining a constant roll (~25°) and incidence angle (~29°). Figure 12 shows σ_o versus the ER-2 heading angle from this turn. The nearest available buoy (FWYF1 at 25.59°N, 80.10°W) measured a 3.3 m s^{-1} wind 57° from the north. The radar beam scanned in the cross-track plane, which was 90° from the ER-2 heading. Therefore, the radar beam was pointing approximately upwind when the ER-2 heading angle was 227°. As evident in Fig. 12, σ_o reached its maximum when the radar beam was close to upwind and a minimum when the radar beam was pointing in the crosswind direction. These observations are in general agreement with the measurements

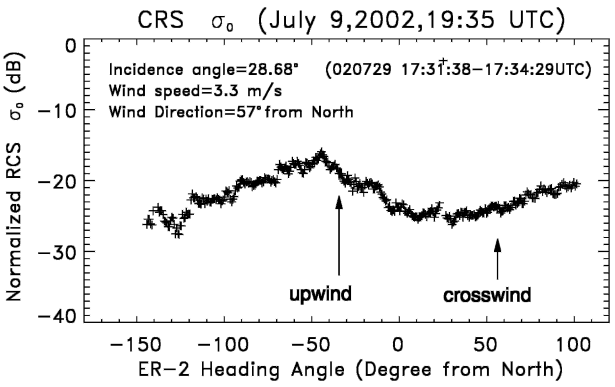

FIG. 12. The σ_o vs ER-2 heading angle.

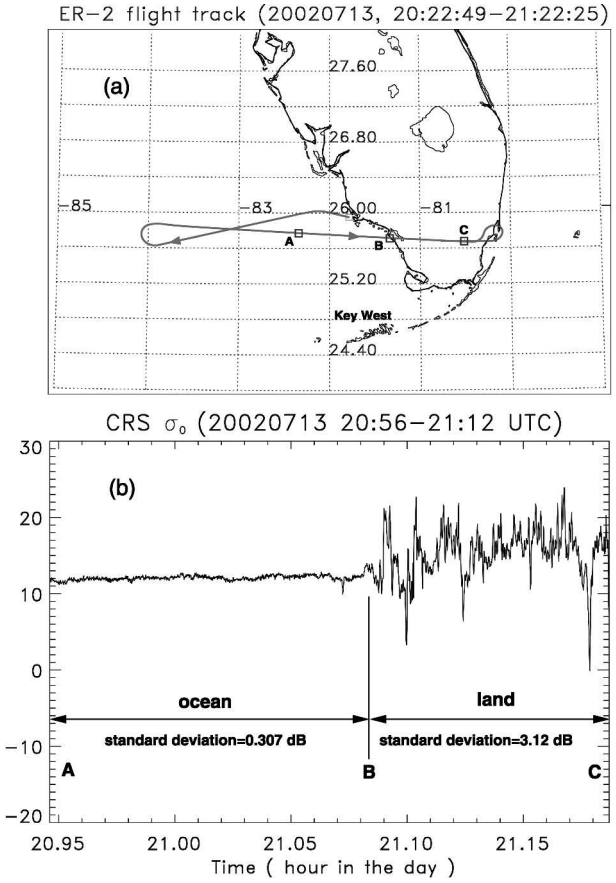

FIG. 13. (a) ER-2 flight track on 13 Jul 2002, which crossed the coastline at point B (2104:53 UTC). (b) The σ_o measured by the CRS from 2056 to 2112 UTC. From the ocean to inland, it shows significant increase in the standard deviation of σ_o.

made by Jones et al. (1976) at 13.9 GHz. Note that the offset between the σ_o maximum and the upwind direction is likely due to a small wind direction error since the buoy was about 22 km away from the center of the turn.

c. Comparison of ocean and land surface return

The CRS-measured surface returns were highly variable over different surface conditions (topography, vegetation, etc.). Compared to terrestrial topography, the ocean surface is more homogeneous, and thus the ocean surface return is less variable. Figure 13a shows an ER-2 flight leg (2022:49–2122:25 UTC) on 13 July 2002 covering ocean and land backgrounds, while Fig. 13b shows the measured sea surface σ_o between points A and C of this line (2056–2112 UTC). Between point A (2056:46 UTC) and point B (2104:53 UTC), where the ER-2 was flying over the ocean, the standard deviation of σ_o is about 0.307 dB; the standard deviation for the inland flight portion (point B to point C) is 3.12 dB. This significant increase in the standard deviation of σ_o is due to the irregularity of the topography and possibly speckle reflection from natural or man-made objects. Since we know that the radar beam incidence angle did not vary significantly during the flight path, the transition point between ocean and land can be found by examining the standard deviation of σ_o measurements. By combining this information with navigational data, the radar beam-pointing angle in the along-track plane at the ocean–land crossing point then can be estimated. One of the practical applications of this method is to determine the approximate pointing direction of the beam for a spaceborne cloud radar.

5. Conclusions

In this paper, we have examined the possibility of using the ocean surface as a calibration reference for airborne and spaceborne millimeter-wave cloud radars. During CRYSTAL-FACE, ocean surface backscattering measurements were obtained using the 94-GHz CRS airborne cloud radar. The CRS was calibrated on the ground using a trihedral corner reflector and by intercomparing measurements with another well-calibrated ground-based radar (Li et al. 2004). The uncertainty of this ground-based calibration is estimated to be 1 dB. This calibration was then applied to deriving estimates of the normalized ocean surface backscatter cross-section σ_o from the surface return. Attenuation due to water vapor and oxygen absorption is estimated and corrected using a Liebe millimeter-wave propagation model and the meteorological data collected by the ER-2 dropsondes.

In our study, the initial CRS measurements confirm that the σ_o is insensitive to surface wind conditions near a 10° incidence angle, a finding similar to what has been found in the literature for lower frequencies. The σ_o measured by the CRS is also compared with a quasi-specular ocean surface scattering model using different surface slope relationships. The results show good agreement between the theoretical models and the measurements at low incidence angles. With these promising results, the analyses in this paper support the proposition of using the ocean surface as a calibration reference for airborne and spaceborne millimeter-wave cloud radars. In addition, the CRS measurements show that the dependence of σ_o on surface wind direction is in general agreement with the measurements made at lower microwave frequencies. The surface wind measurements required for model validation were sparse

during CRYSTAL-FACE, so additional data, such as measurements of backscattering from the ocean surface or wave tank using well-calibrated 94-GHz radars, are necessary to verify and refine the model for different geographic locations and surface wind conditions. We are planning such measurements using CRS during the upcoming experiments. And we hope to make more detailed comparisons with different models, including the quasi-specular model and Plant's multiscale model.

When applying an ocean backscattering model to the calibration of airborne or spaceborne cloud radars, errors may result from the uncertainties in surface wind measurements, atmospheric attenuation estimate, sampling of the peak surface return, and surface temperature measurements. Therefore, proper strategies need to be considered. First, our current study confirms that the σ_o is insensitive to surface wind conditions near a 10° incidence angle. Pointing the radar beam at 10° incidence angle will help to minimize the calibration error due to the possible uncertainties in wind speed measurements. Second, at 94 GHz, the attenuation due to water vapor and oxygen absorption varies significantly from geographic regions and seasons. According to Clothiaux et al. (1995), the two-way PIA is about 0.5 dB for a standard polar winter atmosphere and 2.0 dB for a standard polar summer. For midlatitude areas, this attenuation is about 1.0 dB during winter and 2.8 dB during summer. As we showed in this study, this attenuation could be as high as 7.5 dB for tropical ocean areas and varied over a range of 2.5 dB. To reduce the uncertainty in calibration, it is essential to conduct the calibration under the most favorable atmospheric conditions, such as over the midlatitude ocean during the winter season. Third, cloud radars are usually designed for best detection of volume targets, such as clouds. a proper detection method has to be used to minimize the error in determining the peak return from a surface target, such as the ocean. Our studies confirm that oversampling significantly reduces the error of surface return measurements. Finally, the variation of surface temperature affects the value of Fresnel reflection coefficient $\Gamma(0, \lambda)$, which varies from 0.60 for 10°C to 0.64 for 20°C seawater. This corresponds to a 0.5-dB change in σ_o calculation. It is therefore necessary to obtain accurate measurements of surface temperature within the radar beam footprint. With the above uncertainties minimized, the use of the ocean surface shows promise for achieving a calibration accuracy of 2–3 dB. For spaceborne measurements, averaging of many measurements from global datasets will further reduce errors.

Acknowledgments. The CRS measurements during NASA CRSYSTAL-FACE were supported by Dr. Don Anderson and the Radiation Science Program at NASA Headquarters. Thanks to Ed Zenker and Dr. Steve Bidwell for their help in the CRYSTAL-FACE field effort; to the NASA ER-2 crew and pilots for their support during the CRS installation, test flight and field experiment; to Dr. Steve Sekelsky and Eric Knapp of the University of Massachusetts for their help during the CRS/CPRS intercomparison; to Dr. Jeffrey Halverson for providing ER-2 dropsonde data; to Dr. Robert Meneghini for instructive discussions; and to Dr. William Plant for his help on the multiscale ocean surface backscattering model.

APPENDIX

Estimate of Correction Factor C_e

For a smooth surface, the Fresnel reflection coefficient at normal incidence is given by the classic formula as $\Gamma(0, \lambda) = [n(\lambda)-1.0]/[n(\lambda) + 1.0]$where $n(\lambda)$ is the complex refractive index of the surface materials (Ulaby et al. 1981). At 94 GHz, $|\Gamma(0, \lambda = 3 \text{ mm})|^2 = 0.409$ for a smooth ocean surface. However, the ocean surface is generally roughened by gravity waves, surface winds, and precipitation. According to Jackson et al. (1992), small-scale surface roughness diffracts the incident radiation. This diffractive process reduces the Fresnel reflection coefficient. It is therefore necessary to use the effective Fresnel reflection coefficient $\Gamma_e(0, \lambda) = C_e[n(\lambda)-1.0]/[n(\lambda) + 1.0]$, where C_e accounts for the surface roughness effects. Here, C_e is generally smaller than 1 and is equal to 1 only for a perfectly smooth surface.

Based on the statistical analysis of the ocean surface backscattering measurements obtained by the Tropical Rainfall Measuring Mission K_u-band (13.8 GHz) spaceborne radar, Freilich and Vanhoff (2003) estimated that C_e is approximately 0.89 for surface wind speed between 1.5 and 15 m s^{-1}. At 94 GHz, estimates of C_e have been difficult to obtain due to the lack of measurements of the ocean surface. Here, we compare σ_o calculated from (4) and σ_o measured by the CRS to estimate C_e. At low incidence angle (near nadir), σ_o is not useful for estimating C_e because it is sensitive to different $s(v)^2$ empirical relationships and has relatively large variability with surface wind speed at nadir. However, at a 10° incidence angle, σ_o is insensitive to surface wind speed and to $s(v)^2$ empirical relationships for $3.0 < v < 10.0$ m s^{-1}. The mean value of σ_o calculated within this wind speed range ($3.0 < v < 10.0$ m s^{-1}) for all three $s(v)^2$ relationships is $6.94 + 20 \log (C_e)$ dB. The

σ_o measurements at 10° incidence angles obtained by the CRS from different turn events have a mean value of 5.85 dB and a standard deviation of 0.6 dB. By comparing σ_o calculated from the model with these measured by the radar, C_e is estimated to be 0.88 with an uncertainty of 0.16. Errors in system calibration, σ_o calculation, and atmospheric attenuation estimates are possible sources of the uncertainty in C_e. This C_e estimate is almost the same as the TRMM estimate, but it does not necessarily mean that C_e is frequency independent. More experimental data are necessary to examine the dependency of C_e on radar frequencies.

REFERENCES

Barrick, D. E., 1974: Wind dependence of quasi-specular microwave sea scatter. *IEEE Trans. Antennas Propag.,* **22,** 135–136.

Brown, G., 1978: Backscattering from a Gaussian-distributed perfectly conducting rough surface. *IEEE Trans. Antennas Propag.,* **26,** 472–482.

——, 1990: Quasi-specular scattering from the air–sea interface. *Surface Waves and Fluxes*, Vol. 2, W. Plant and G. Geernart, Eds., Kluwer Academic, 1–40.

Caylor, I. J., G. M. Heymsfield, R. Meneghini, and L. S. Miller, 1997: Correction of sampling errors in ocean surface cross-sectional estimates from nadir-looking weather radar. *J. Atmos. Oceanic Technol.,* **14,** 203–210.

Chan, H. L., and A. K. Fung, 1977: A theory of sea scatter at large incident angles. *J. Geophys. Res.,* **82,** 3439–3444.

Clothiaux, E., M. Miller, B. Albrecht, T. Ackerman, J. Verlinde, D. Babb, R. Peters, and W. Syrett, 1995: An evaluation of a 94-Ghz radar for radar remote sensing of cloud properties. *J. Atmos. Oceanic Technol.,* **12,** 201–229.

Cox, C., and W. Munk, 1954: Measurements of the roughness of the sea surface from photographs of the sun's glitter. *J. Opt. Soc. Amer.,* **144,** 838–850.

European Space Agency, 2001: EarthCARE—Earth Clouds, Aerosols and Radiation Explorer. Five Candidate Earth Explorer Core Missions Assessment Rep. SP-1257(1), ESA Publication Division, Noordwijk, Netherlands, 135 pp.

Freilich, M. H., and B. A. Vanhoff, 2003: The relationship between winds, surface roughness, and radar backscatter at low incidence angles from TRMM precipitation radar measurements. *J. Atmos. Oceanic Technol.,* **20,** 549–562.

Heymsfield, G. M., and Coauthors, 1996: The EDOP radar system on the high-altitude NASA ER-2 aircraft. *J. Atmos. Oceanic Technol.,* **13,** 795–809.

——, B. Geerts, and L. Tian, 2000: TRMM precipitation radar reflectivity profiles as compared with high-resolution airborne and ground-based radar measurements. *J. Appl. Meteor.,* **39,** 2080–2102.

Hock, T. F., and J. L. Franklin, 1999: The NCAR GPS dropsonde. *Bull. Amer. Meteor. Soc.,* **80,** 407–420.

Houghton, J. T., L. G. Meira Filho, B. A. Callander, N. Harris, A. Kattenberg, and K. Maskell, Eds., 1996: *Climate Change 1995*: *The Science of Climate Change*. Cambridge University Press, 572 pp.

Iguchi, T., and R. Meneghini, 1994: Intercomparison of single-frequency methods for retrieving a vertical rain profile from airborne or spaceborne radar data. *J. Atmos. Oceanic Technol.,* **11,** 1507–1516.

Jackson, F. C., W. T. Walton, and D. E. Hines, 1992: Sea surface mean square slope from Ku-band backscatter data. *J. Geophys. Res.,* **97,** 11 411–11 427.

Jones, W. L., L. C. Schroeder, and J. L. Michell, 1976: Aircraft measurements of the microwave scattering signature of the ocean. *IEEE Trans. Antennas Propag.,* **25,** 52–61.

Kozu, T., 1995: A generalized surface echo radar equation for down-looking pencil beam radar. *IEICE Trans. Commun.,* **E78B,** 1245–1248.

——, S. Satoh, H. Hanado, T. Manabe, M. Okumura, K. Okamoto, and T. Kawanishi, 2000: Onboard surface detection algorithm from TRMM precipitation radar. *IEICE Trans. Commun.,* **E83B,** 2021–2031.

Lhermitte, R., 1988: Cloud and precipitation remote sensing at 94 GHz. *IEEE Trans. Geosci. Remote Sens.,* **26,** 1069–1089.

Li, L., and Coauthors, 2001: Retrieval of atmospheric attenuation using combined ground-based and airborne 95-GHz cloud radar measurements. *J. Atmos. Oceanic Technol.,* **18,** 1345–1353.

——, G. M. Heymsfield, P. E. Racette, L. Tian, and E. Zenker, 2004: A 94-GHz cloud radar system on a NASA high-altitude ER-2 aircraft. *J. Atmos. Oceanic Technol.,* **21,** 1378–1388.

Liebe, H., 1985: An updated model for millimeter-wave propagation in moist air. *Radio Sci.,* **20,** 1069–1089.

Masuko, H., K. Okamoto, M. Shimada, and S. Niwa, 1986: Measurements of microwave backscattering signatures of the ocean surface using X-band and Ka band airborne scatterometers. *J. Geophys. Res.,* **91,** 13 065–13 083.

McGill, M. J., and Coauthors, 2004: Combined lidar–radar remote sensing: Initial results from CRYSTAL-FACE. *J. Geophys. Res.,* **109,** D07203, doi:10.1029/2003JD004030.

Meneghini, R., and T. Kozu, 1990: *Spaceborne Weather Radar*. Artech House, 199 pp.

——, J. Eckerman, and D. Atlas, 1983: Determination of rain rate from a spaceborne radar using measurements of total attenuation. *IEEE Trans. Geosci. Remote Sens.,* **21,** 34–43.

Pazmany, A. L., R. E. McIntosh, R. Kelly, and G. Vali, 1994: An airborne 95-GHz dual polarization radar for cloud studies. *IEEE Trans. Geosci. Remote Sens.,* **1,** 731–739.

Plant, W. J., 1977: Studies of backscatter sea return with a CW, dual-frequency, X-band radar. *IEEE Trans. Antennas Propag.,* **25,** 28–36.

——, 2002: A stochastic, multiscale model of microwave backscatter from the ocean. *J. Geophys. Res.,* **107,** 3120, doi:10.1029/2001JC000909.

Sadowy, G. A., and Coauthors, 1997: The NASA DC-8 airborne cloud radar: Design and preliminary results. *Proc. Int. Geoscience and Remote Sensing Symp.*, Vol. 4, Singapore, Singapore, IEEE, 1466–1469.

Sekelsky, S. M., 2002: Near field reflectivity and antenna boresight gain corrections for millimeter-wave atmospheric radars. *J. Atmos. Oceanic Technol.,* **19,** 468–477.

——, and R. E. McIntosh, 1996: Cloud observations with polarimetric 33 GHz and 95 GHz radar. *Meteor. Atmos. Phys.,* **59,** 123–140.

Stephens, G. L., S. C. Tsay, P. W. Stackhouse, and P. J. Flatau, 1990: The relevance of the microphysical and radiative properties of cirrus clouds to climate and climate feedback. *J. Atmos. Sci.,* **47,** 1742–1752.

——, and Coauthors, 2002: The CloudSat mission and the A-Train. *Bull. Amer. Meteor. Soc.,* **83,** 1771–1790.

Ulaby, F. T., R. K. Moore, and A. K. Fung, 1981: *Microwave Remote Sensing*: *Active and Passive.* Vol. 1. Artech House, 456 pp.

Valenzuela, G. R., 1978: Theories for the interaction of electromagnetic and oceanic waves—A review. *Bound.-Layer Meteor.,* **13,** 61–85.

Wu, J., 1972: Sea-surface slope and equilibrium wind–wave spectra. *Phys. Fluids,* **15,** 741–747.

——, 1990: Mean square slopes of the wind disturbed water surface, their magnitude, directionality, and composition. *Radio Sci.,* **25,** 37–48.